PHYSICAL REVIEW E VOLUME 53, NUMBER 3 MARCH 1996

Implicit-moment, partially linearized particle simulation of kinetic plasma phenomena

Bruce I. Cohen, Andris M. Dimits, and John J. Stimson*
Lawrence Livermore National Laboratory, University of California, Livermore, California 94550

D. C. Barnes
Los Alamos National Laboratory, University of California, Los Alamos, New Mexico 87545

(Received 18 September 1995)

An algorithm for kinetic simulation of electron and ion plasmas is introduced that combines both implicit and perturbative methods to deal efficiently with disparate time scales and signal-to-noise issues associated with particle discreteness. The algorithm is introduced for an electrostatic model in a strong magnetic field with gyrokinetic ions and drift-kinetic electrons. Some of the numerical dispersion properties are analyzed and confirmed in test simulations. Two-dimensional applications of the algorithm to drift-wave instabilities excited either by an ion temperature gradient (ion-temperature-gradient instability) or by electron inverse Landau damping in the presence of a density gradient (collisionless drift instability) are presented that illustrate the usefulness of the method. Clear gains in resolution and computational efficiency over previous methods are achieved.

PACS number(s): 52.65.−y, 52.35.Qz, 02.70.−c

I. INTRODUCTION

Because plasma phenomena in laboratory and space plasmas exhibit such a wide range of disparate time scales, the field of plasma simulation has been rich in the invention of techniques that take advantage of disparate time scales to achieve an improvement in computational efficiency [1]. This work presents progress in the development of efficient algorithms for the kinetic simulation of electron and ion plasmas. The particular methods applied here represent a combination of multiple-time-scale techniques that have been found successful when used separately.

A more specific goal of this work is the efficient simulation of electrostatic drift-wave turbulence in a strongly magnetized plasma excited by instabilities in which both electron and ion kinetic effects are potentially important. We specialize further to a class of drift-wave instabilities that are important in the core of tokamaks [2] for which the mode frequency ω is much less than the ion cyclotron frequency Ω_i, $\omega \ll \Omega_i$, the wave number parallel to the magnetic field **B** is much smaller than that perpendicular to **B**, the product of the ion Larmor radius ρ_i and the perpendicular wave number $k_\perp$ satisfies $k_\perp \rho_i \le O(1)$, and the electron Larmor radius is much smaller than any of the lengths of interest.

Our algorithm combines the features of the following kinetic algorithms. To simulate drift waves with $\omega \ll \Omega_i$ while retaining ion Larmor radius effects, we adopt Lee's gyrokinetic description of the ions [3]. We model the electrons with drift-kinetic equations of motion ($\mathbf{E}\times\mathbf{B}$ motion across the magnetic field and full parallel dynamics). We assign a time step to the electrons that is an integer submultiple of the ion time step so that the electrons can be subcycled [4] and orbit averaged [5] to accommodate their transit along the magnetic field, which is faster than the ions. To model tokamak core turbulence in plasmas that are weakly perturbed from a Maxwellian, we use a partially linearized (δf) representation for both electrons and ions [6,7]. For small perturbations, the δf method achieves a large reduction in the number of particles needed for kinetic simulation. Finally, we introduce implicit-moment equations as an intermediary between the electrons and Poisson's equation to determine the self-consistent electric fields so that the field solution is implicit and suppresses unwanted high-frequency modes and thermal noise [8–10]. The stability of the resulting algorithm is relatively robust compared to that experienced with semi-implicit methods in fully nonlinear simulations with gyrokinetic ions and drift-kinetic electrons [11].

The combination of implicit-moment equations and δf methods was introduced in earlier work by Barnes and Nebel [12], which accommodated the evolution of the background density, momentum flux, and temperature in fluid equations with the constraints that the corresponding first three moments of the perturbed velocity distribution vanish. Barnes has called this the quiet-implicit particle-in-cell method [12]. The quiet-implicit work differs from the work described here in that in this work the background velocity distribution is a fixed, nondrifting Maxwellian; the first three moments of the perturbed distribution function are *not* constrained to vanish, and in the applications to two-dimensional drift-wave turbulence presented, the ions are gyrokinetic and the electrons are drift kinetic.

This paper is organized as follows. In Sec. II is presented a detailed description of our implicit-moment δf algorithm and some of its attributes. We present several test cases in Sec. III, including simulations of the cold-electron ω_h mode (the highest frequency mode sup-

---

*Present address: Cornell University, Ithaca, NY.

ported by our model) with an analysis of its numerical dispersion and stability for finite time step, the warm-electron ω_h mode with electron Landau damping, the ion-temperature-gradient (ITG) instability, and the collisionless-drift instability destabilized by inverse electron Landau damping in the presence of a density gradient. Concluding remarks are presented in Sec. IV. The algorithm performance is quite good. The δf representation of both electrons and ions had excellent signal-to-noise characteristics with modest statistical requirements for the examples considered here. Because of the implicit time integration, limitations on time step were set by accuracy considerations rather than by the numerical stability of the ω_h mode.

II. IMPLICIT-MOMENT δf ALGORITHM

The electrostatic implicit-moment δf algorithm in a magnetically sheared slab consists of the following elements. The ions satisfy the reduced Vlasov-Poisson equations [3] based on the following standard gyrokinetic ordering:

$$\frac{\delta f}{F_M} \sim \frac{q_i \phi}{T_i} \sim \frac{\omega}{\Omega_i} \sim \frac{\rho_i}{L} \sim \epsilon \ll 1, \quad L \sim L_\| ,$$

where $\rho_i \equiv v_i/\Omega_i$, $\Omega_i \equiv q_i B/m_i c$, $v_i \equiv \sqrt{T_i/m_i}$, q_i, m_i, and T_i are, respectively, the ion charge, mass, and temperature, c is the speed of light, B is the magnetic field strength, ϕ is the electrostatic potential, ω is the frequency of the perturbation, L is a characteristic perpendicular equilibrium scale length of the system, and $L_\|$ is the characteristic parallel wavelength of the perturbation.

The electrostatic gyrokinetic Vlasov equation for a plasma in a uniform magnetic field is [13,14]

$$\frac{\partial \delta f}{\partial t} + v_\| \hat{\mathbf{b}} \cdot \frac{\partial \delta f}{\partial \mathbf{R}} - \frac{c}{B} \frac{\partial}{\partial \mathbf{R}} \cdot \left\{ \left[\frac{\partial \bar{\phi}}{\partial \mathbf{R}} \times \hat{\mathbf{b}} \right] \delta f \right\}$$
$$= -\frac{q v_\|}{T} \frac{\partial \bar{\phi}}{\partial \mathbf{R}} \cdot \hat{\mathbf{b}} F_M - \kappa \frac{c}{B} \frac{\partial \bar{\phi}}{\partial y} F_M + C(\delta f) , \qquad (1a)$$

where $\kappa \equiv -\nabla \ln F_M$, F_M is an equilibrium Maxwellian distribution function,

$$\bar{\phi} \equiv \frac{1}{2\pi} \int d\hat{\boldsymbol{\rho}}\, \phi(\mathbf{R} + \boldsymbol{\rho}) , \qquad (1b)$$

$\mathbf{R} \equiv \mathbf{x} - \boldsymbol{\rho}$, $\boldsymbol{\rho} \equiv \mathbf{v}_\perp \times \hat{\mathbf{b}}$, $\hat{\boldsymbol{\rho}}$ is a unit vector in the direction of $\boldsymbol{\rho}$, $\mathbf{x}$ is the particle position, $\mathbf{v}_\perp$ is the perpendicular velocity, $\delta f(\mathbf{R}, \mu, v_\|, t)$ is the gyroaveraged perturbed distribution function, $\mu \equiv v_\perp^2/2$, and $C(F)$ is a collision operator. The electrostatic potential ϕ is given by the gyrokinetic Poisson equation which, for a single ion species i, is

$$\nabla^2 \phi - \frac{\tau(\phi - \tilde{\phi})}{\lambda_D^2} = -4\pi e(\bar{n}_i - n_e) , \qquad (1c)$$

where

$$\tilde{\phi}(\mathbf{x}) \equiv \frac{1}{2\pi} \int d\mu\, d\hat{\boldsymbol{\rho}}\, \bar{\phi}(\mathbf{x} - \boldsymbol{\rho}) , \qquad (1d)$$

$$\bar{n}(\mathbf{x}) \equiv \int d\mu\, dv_\|\, d\hat{\boldsymbol{\rho}}\, \delta f(\mathbf{x} - \boldsymbol{\rho}, \mu, v_\|, t) , \qquad (1e)$$

and where $\tau \equiv T_e/T_i$, $\rho_s \equiv c_s/\Omega_i$, $c_s \equiv \sqrt{T_e/m_i}$, $k_\perp$ is the perpendicular wave number, $\lambda_D \equiv \sqrt{T_e/4\pi n_0 e^2}$ is the electron Debye length, and n_0 is the background ion number density. The angle integrations of Eqs. (1b) and (1e) are replaced by averages over four points on a ring, combined with a charge-deposition or field-interpretation calculations involving spatial weighting functions [3].

The term on the right-hand side of Eq. (1a) containing κ represents the radial $\mathbf{E} \times \mathbf{B}$ advection from an equilibrium with gradients in the radial direction. In the presence of density and temperature gradients, for example, $\kappa = \kappa_n \{1 + \eta(v^2/2v_i^2 - 3/2)\}$, where $\eta \equiv (d \ln T_0 / d \ln n_0)$ and κ_n represents the density gradient. Here, $\partial/\partial x$ represents a derivative in the direction of the equilibrium gradients and $\partial/\partial y$ represents a derivative in the direction perpendicular to the magnetic field and the equilibrium gradients. In slab geometry, the magnetic field has its principal component in the z direction with amplitude B_0 and has a small component in the y direction. With no shear $B_y = \text{const}$ and with shear $B_y = B_0(x - x_0)/L_s$ where L_s is the magnetic shear length.

The term "partially linearized" denotes the fact that there is no parallel acceleration nonlinearity in Eq. (1a). This fact is used in the partially linearized particle simulation method by recognizing that the characteristics of Eq. (1a) preserve any spatially uniform particle distribution. In addition, we employ a linearized multiscale method so that the effects of density and temperature nonuniformity appear only through κ on the right-hand side of Eq. (1a) and similarly for the electrons. The $k_x = 0$ components of ϕ are suppressed. A particle method is then introduced to solve Eq. (1a):

$$\delta f = \sum_j w_j(t) \delta(\mathbf{R} - \mathbf{R}_j) \delta(v_\| - v_{\| j}) \delta(\mu - \mu_j) , \qquad (2)$$

where $\mathbf{R}_j$ and $v_{\| j}$ evolve according to the characteristic equations of Eq. (1a). In the absence of collisions, if the simulation particles j are loaded as a uniform Maxwellian then the source terms on the right-hand side of Eq. (1a) are correctly taken into account if w_j evolves according to

$$\dot{w}_j = -\frac{q v_\|}{T} \frac{\partial \bar{\phi}}{\partial \mathbf{R}} \cdot \hat{\mathbf{b}} - \kappa \frac{c}{B} \frac{\partial \bar{\phi}}{\partial y}$$

along the characteristics. In our implementation, a second-order-accurate predictor-corrector time integration of the ion equations of motion is used with a time step Δt_i. A four-point gyroaveraged ion charge deposition is computed on both predictor and corrector steps.

The partially linearized method is a special case of the more general "δf method," which allows for different choices of particle loading, for the inclusion of nonlinearities such as the parallel acceleration nonlinearity that become important when $\delta f/F_M \ll 1$ no longer holds for arbitrary analytically described sources [6], and for compressibility in the phase-space characteristics [15]. A generalization of the partially linearized method to include the parallel nonlinearity has also been given by Parker and Lee [16].

The electrons satisfy a drift-kinetic Vlasov equation that can be obtained from Eq. (1a) and Eq. (2) by replacing ion quantities with electron quantities and taking the limit of zero electron Larmor radius. No gyroaveraging is required in computing forces on the electrons (computed at the electron gyrocenter) or in depositing their charge density or any other moment on the spatial grid. The electron particle motion is calculated basically using the same predictor-corrector algorithm as the ions but with a time step Δt_e that is a submultiple of the ion time step. A sequence of electron advances is calculated over a number of electron time steps adding up to the ion time step. The self-consistent electric field is updated on the ion time step. The motivation for subcycling [4] the electron advance is that with a realistic ion-to-electron mass ratio, the parallel electron transit motion is typically much faster than that of the ions because $v_e \gg v_i$ where $v_e \equiv \sqrt{T_e/m_e}$ and $v_i \equiv \sqrt{T_i/m_i}$.

At this point, the Poisson equation (1c) could be solved using an explicit electron charge density n_e computed synchronously with the gyroaveraged ion charge density $\bar{n}_i$. However, we will introduce implicit-moment equations for the electrons in order to remove undesirable high-frequency modes, reduce the thermal noise associated with these high-frequency modes, and ensure numerical stability. The implicit-moment equations for the perturbed electron quantities are computed from the partially linearized drift-kinetic Vlasov equation:

$$\frac{\partial \delta f_e}{\partial t} + v_{\parallel} \hat{\mathbf{b}} \cdot \nabla \delta f_e + \mathbf{v}_{\mathbf{E}\times\mathbf{B}} \cdot \nabla \delta f_e - \frac{e v_{\parallel}}{m_e v_e^2} F_{Me} \hat{\mathbf{b}} \cdot \nabla \phi + \frac{c}{B} \frac{\partial \phi}{\partial y} \frac{F_{Me}}{L_{Te}} \left[\frac{L_{ne}}{L_{Te}} + \frac{v_{\parallel}^2}{2 v_{\perp}} - \frac{1}{2} \right] = 0 \ . \tag{3}$$

In finite-difference form for the time derivatives, the moment equations for the *perturbed* electron moments derived from Eq. (3) are

$$\frac{n_e^{n+1} - n_e^n}{\Delta t_i} + \nabla_{\parallel} [\epsilon_1 j_{e\parallel}^{n+1} + (1-\epsilon_1) j_{e\parallel}^n] = -\frac{n_0 e v_{*e}}{T_e} \frac{\partial}{\partial y} [\epsilon_1 \phi^* + (1-\epsilon_1)\phi^n] - (\mathbf{v}_{\mathbf{E}\times\mathbf{B}} \cdot \nabla_{\perp} n_e)^{**} \ , \tag{4}$$

$$\begin{aligned} \frac{j_{e\parallel}^{n+1} - j_{e\parallel}^n}{\Delta t_i} &+ v_e^2 \nabla_{\parallel} [\epsilon_2 n_e^{n+1} + (1-\epsilon_2) n_e^n] - \frac{e n_0}{m_e} \nabla_{\parallel} [\epsilon_2 \phi^{n+1} + (1-\epsilon_2)\phi^n] + \nu_{ei} [\epsilon_2 j_{e\parallel}^{n+1} + (1-\epsilon_2) j_{e\parallel}^n] \\ &= [-\mathbf{v}_{\mathbf{E}\times\mathbf{B}} \cdot \nabla_{\perp} j_{e\parallel} + \nu_{ei} \bar{\mathbf{j}}_{i\parallel} - \nabla_{\parallel} (p_{e\parallel}^{n+1/2} - n_e v_e^2)]^{**} \ , \end{aligned} \tag{5}$$

where n_e is the electron number density, $j_{e\parallel}$ is the electron parallel current density per unit charge, (i.e., the parallel flux density, $\mathbf{v}_{\mathbf{E}\times\mathbf{B}}$ is the $\mathbf{E}\times\mathbf{B}$ velocity at the electron gyrocenter, $v_{*e} \equiv (\rho_e / L_{ne}) v_e$, ν_{ei} is the electron-ion collision rate, $p_{e\parallel} \equiv \langle v_{e\parallel}^2 \rangle$ is the parallel pressure moment computed on the electron velocity distribution function, $j_{e\parallel}$ is the electron parallel flux density, $j_{i\parallel}$ is the corresponding ion parallel flux density that must be computed if $\nu_{ei} \neq 0$, and $\epsilon_1, \epsilon_2, \epsilon_3$ are centering parameters $(0 \le \epsilon_i \le 1)$. The superscripts indicate electron time levels with the $*$ denoting time level n on the predictor pass and the predicted value at time level $n+1$ on the corrector pass in advancing quantities from time $n\Delta t_i$ to time $(n+1)\Delta t_i$. The $**$ superscript denotes evaluation at time level n on the predictor pass and the average of values at time levels n and $n+1$ on the corrector pass.

The moment equations are bound to the particle electrons by setting the number and flux densities n_e^n and $j_{e\parallel}^n$ in Eqs. (4) and (5) equal to the corresponding particle moments accumulated on the spatial mesh. The electron parallel pressure moment is an orbit-averaged moment [5] computed from the simple average over the time interval $n\Delta t_i$ to $(n+1)\Delta t_i$ of the parallel electron pressure moment per unit mass accumulated at each Δt_e. The electron particle equations of motion are advanced in a predictor step from $n\Delta t_i$ to $(n+1)\Delta t_i$ using the electric and magnetic fields at $n\Delta t_i$ interpolated to the electron trajectories computed with Δt_e. The ions are advanced in one big predictor step from $n\Delta t_i$ to $(n+1)\Delta t_i$, and the gyroaveraged ion moments are computed before solving for the predicted fields at $(n+1)\Delta t_i$. On the corrector pass, the electrons are again advanced from $n\Delta t_i$ to $(n+1)\Delta t_i$, but $\phi^* = \epsilon_3 \phi^{n+1} + (1-\epsilon_3)\phi^n$ is used to calculate forces and drifts. To have the electron fluid and particle motion synchronized as much as possible, we usually set $\epsilon_3 = \epsilon_2$. The entire scheme is accurate to $O(\Delta t_i^2)$ if $\epsilon_1 = \epsilon_2 = 1/2$.

Equations (4) and (5) are a linear system of equations for n_e^{n+1} and $j_{e\parallel}^{n+1}$ that is solved exactly and whose result for n_e^{n+1} is then substituted into Eq. (1c) to determine ϕ^{n+1}. This renders the Poisson equation implicit because n_e^{n+1} depends linearly on ϕ^{n+1}. It is important to note that in an electromagnetic model, both ϕ and $A_{\parallel}$ would contribute to $E_{\parallel}$ in the equations of motion and on the right-hand side of Eq. (5), and the expression for $j_{e\parallel}$ would be substituted into Ampere's equation. Ampere's and Poisson's equations would provide a coupled linear system for ϕ and $A_{\parallel}$ [17].

The solution of the implicit gyrokinetic Poisson equation in a magnetically sheared domain requires some special measures. For applications to tokamak core turbulence $\omega_{pi}^2/\Omega_i^2 \gg 1$ and the vacuum polarization is negligible. Here, ω_{pi} is the ion plasma frequency and Ω_i is the ion cyclotron frequency. Poisson's equation becomes a statement of quasineutrality and takes the form

$$\left\{\frac{\omega_{pi}^2}{\Omega_i^2}\frac{1-\Gamma_0(b)}{\rho_i^2}+C\omega_{pe}^2\Delta t_i^2 k_\parallel^2(x)\right\}\phi(k_y,x)=S(k_y,x)\ , \tag{6}$$

where $b=k_\perp^2\rho_i^2$, $\Gamma_0(b)=I_0(b)\exp(-b)$, I_0 is the modified Bessel function, $C\equiv\epsilon_1\epsilon_2/(1+\epsilon_1\epsilon_2 k_\parallel^2 v_e^2\Delta t_i^2)$, and $k_\perp^2=k_y^2-\partial^2/\partial x^2$. The Poisson equation (6) can be conveniently solved with a Padé approximation: $1-\Gamma_0(b)\approx b/(1+b)$, a Fourier transform in y, and finite differencing in x leading to a tridiagonal matrix inversion. With $b=\rho_i^2(k_y^2-\partial^2/\partial x^2)$ and $C'\equiv C(\Omega_i^2/\omega_{pi}^2)\omega_{pe}^2\Delta t_i^2$, Eq. (6) becomes

$$[k_\perp^2+(1+b)C'k_\parallel^2(x)]\phi(k_y,x)=\frac{\Omega_i^2}{\omega_{pi}^2}(1+b)S(k_y,x)\ . \tag{7}$$

We formally invert the operator on the left-hand side of Eq. (7), collect the $\partial^2/\partial x^2$ terms, and perform a long division to remove $\partial^2/\partial x^2$ from the numerator of the resulting formal solution. The result is that the electrostatic potential satisfying Poisson's equation is given by

$$\phi(k_y,x)=\rho_i^2\psi_2-\frac{\psi_3}{1+C'\rho_i^2k_\parallel^2}\ , \tag{8}$$

where $k_\parallel=k_y(x-x_0)/L_s$, $k_\parallel$ vanishes at x_0, L_s is the magnetic shear length in x, $\psi_2(k_y,x)=(\Omega_i^2/\omega_{pi}^2)S(k_y,x)/(1+C'\rho_i^2k_\parallel^2)$, and ψ_3 satisfies

$$L_1\psi_3(k_y,x)=\psi_2(k_y,x)\ ,$$

$$L_1\equiv\frac{\partial^2}{\partial x^2}-\frac{k_y^2+(1+k_y^2\rho_i^2)C'k_\parallel^2(x)}{1+C'\rho_i^2k_\parallel^2(x)}\ , \tag{9}$$

which requires the inversion of a tridiagonal matrix equation with ψ_2, ψ_3, and ϕ sharing the same boundary conditions in x. One then obtains $\phi(x,y)$ by computing the inverse Fourier transform from $\phi(k_y,x)$. Simple periodic boundary conditions in x and y are used for simulations in an unsheared magnetic field with $B_y=\text{const}$. For B_y a function of x, a bounded simulation model is used with $\phi=0$ at the boundaries in x, and periodic boundary conditions are used in y.

This implicit-moment δf algorithm has the following attributes. The implicitness stabilizes and damps ω_h oscillations at large time step, where $\omega_h^2=(k_\parallel/k_y)^2(m_i/m_e)\Omega_i^2$. The ω_h mode derives from a balance between the ion polarization charge density perturbation and the electron charge density perturbation associated with the parallel electron response [3]. The δf representation reduces the statistical requirements by $O(\delta f/F_M)^2$ over conventional particle simulation methods that represent the entire distribution function with particles [6,7]. Subcycling the electrons allows the use of time steps Δt_i and Δt_e tailored to give good resolution of the particle trajectories while accommodating a realistic mass ratio more efficiently than in the case where the smaller Δt_e is used for both species. Implicitness in the fluid electron pressure in Eq. (5) relaxes a time-step constraint associated with the calculation of the electron pressure, $(B_y/B_0)v_e\Delta t_i/\Delta y<1$, as pointed out by Denavit [8]. Orbit-averaging time centers and smooths the electron pressure accumulation. We expect that the combination of these attributes should make simulations with kinetic electrons and ions more efficient and quieter than traditional particle methods. The test cases presented in the next section were useful in confirming that correct solutions were obtained and demonstrated that this new algorithm can lead to improvements in noise reduction and efficiency.

III. SIMULATION TEST CASES

A. Cold-plasma ω_h mode

The first test of this algorithm is to assess the dispersion of the ω_h mode for a finite time step in a cold plasma. For a cold uniform plasma and fully implicit differencing, $(\epsilon_1=\epsilon_2=\epsilon_3=1)$, the linearized electron fluid equations and particle equations of motion can be solved together with the gyrokinetic Poisson's equations as a linear algebraic system. For this simple case, we consider the limit of $k\Delta x\ll 1$ but retain finite-time-step effects. For $\omega\sim\omega_h\gg k_\parallel v_i$ and $k_\parallel\ll k_\perp$, the parallel ion response is negligible compared to the parallel electron response and the ion polarization response. We introduce $\lambda\equiv\exp(-i\omega\Delta t_i)$ and obtain a dispersion relation from the characteristic equation for the linear system:

$$\lambda^2-2\lambda\left[1-\frac{3}{4}\alpha\right]+1-\frac{\alpha}{2}=0\ , \tag{10}$$

where $\alpha=\omega_h^2\Delta t_i^2/(1+\omega_h^2\Delta t_i^2)$, $N\equiv\Delta t_i/\Delta t_e$, and we have dropped terms of $O(1/N)$, which arise from the sum of the subcycled electron displacements leading to the perturbed electron number density at the end of the ion time step interval, i.e., $\sum_{j=1}^{N}j=N(N+1)/2\approx N^2/2$. On including the $1/N$ corrections, we obtain $|\lambda|^2=1-\alpha/2^*$, where $1/2^*\equiv(1+1/N)/2$, which is stable $(|\lambda|\le 1)$ for all values of $\omega_h^2\Delta t_i^2$ because $0\le\alpha\le 1$. For $\omega_h^2\Delta t_i^2\ll 1$, $\text{Re}\,\omega\approx\pm\omega_h$. The amplification factor for the ω_h mode asymptotes to $|\lambda|^2\to 1-1/2^*$ as $\omega_h^2\Delta t_i^2\to\infty$. Simulation results are shown in Fig. 1 for $m_i/m_e=1837$, $\Delta t_i/\Delta t_e=5$, $16\Delta x\times 16\Delta y$, $B_y/B_0=0.01$, 128×128 particles of each species, cold plasma, and $k_y\Delta y=0.4$. The solutions for $\text{Re}\,\omega\Delta t_i$ and $|\lambda|^2$ in Fig. 1 determined by Eq. (10) agree quite well with the simulation results. At the largest values of $\omega_h\Delta t_i$, the corrections due to finite $1/N$ are easier to observe.

We have also solved the linear dispersion relation for the cold ω_h modes with $\epsilon_1=\epsilon_2=\epsilon_3=\frac{1}{2}$, i.e., a centered implicit time integration. We obtain the following dispersion relation for $\lambda\equiv\exp(-i\omega\Delta t_i)$:

$$\lambda^3+\lambda^2(-2+2\alpha+\alpha/2^*)+\lambda(1-\alpha)+\alpha(1-1/2^*)=0\ , \tag{11}$$

where α has been redefined as $\alpha=\theta^2/2/(1+\theta^2/2)$. We have made a limited study of the solutions of Eq. (11) and found only stable solutions $|\lambda|^2<1$ for $N=4$ and ∞, and

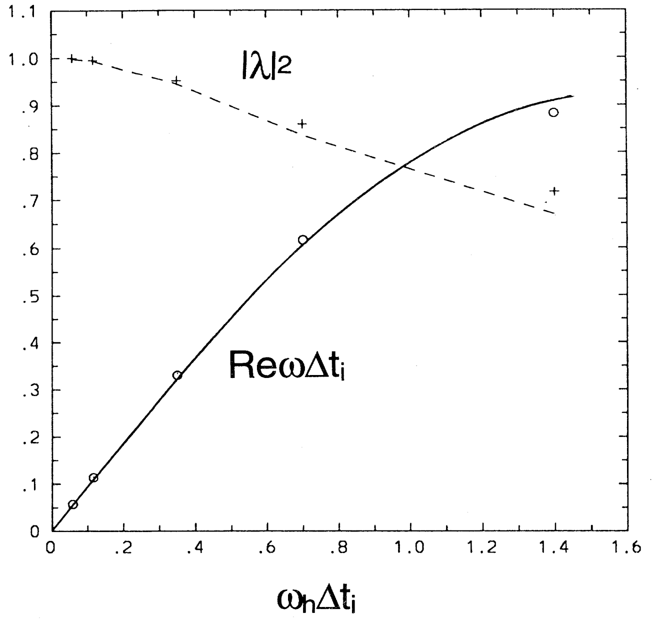

FIG. 1. The dispersion relation for a cold-plasma ω_h mode ($\Delta t_i/\Delta t_e=\infty$ and fully implicit differencing: $\epsilon_1=\epsilon_2=\epsilon_3=1$) and test simulation results with $\Delta t_i/\Delta t_e=5$ for $\mathrm{Re}\,\omega\Delta t_i$ and the amplification factor $|\lambda|^2\equiv|\exp(-i\omega\Delta t_i)|^2$ vs $\omega_h\Delta t_i$. The solid and dotted curves indicate analytical theory.

$|\lambda|$ decreases with increasing $\omega_h\Delta t_i$.

Before continuing on to the other test cases, we comment on a variation of the algorithm. When the electron fluid number and flux densities at the old time level were used in Eqs. (4) and (5) instead of the same quantities accumulated from the electron particle data, a stable well-behaved algorithm results, but discrepancies between the electron fluid and particle-derived charge and flux densities grew secularly; and the simulation tests attempting to confirm electron Landau damping (like those of the next subsection) failed.

B. Warm-plasma ω_h mode: electron Landau damping

A good test of the implicit-moment δf algorithm's accuracy in calculating electron kinetics is the simulation of Landau damping [18]. For this purpose, we excited ω_h modes in a warm plasma at small amplitude by perturbing the initial electron charge density in a single spatial Fourier mode. The asymptotic formulas for the real and imaginary parts of the ω_h mode frequency in the limit of cold ions analogous to the electron plasma wave are

$$\mathrm{Re}\,\omega\approx\sqrt{\omega_h^2+3k_\parallel^2v_e^2}\ , \tag{12}$$

$$\mathrm{Im}\left[\frac{\omega}{\omega_h}\right]=-\sqrt{\pi/8}\left[\frac{\omega_h}{k_\parallel v_e}\right]^3\exp\left[-\frac{\omega^2}{2k_\parallel^2v_e^2}\right]\ . \tag{13}$$

With simulation parameters $\epsilon_1=\epsilon_2=\epsilon_3=0.505$, $16\Delta x\times16\Delta y$, 128×128 particles of each species, $\omega_h\Delta t_i=0.058$, $\Delta t_i/\Delta t_e=5$, $k_y\Delta y=0.4$, and $2\leq\omega_h/k_\parallel v_e\leq5$, very good agreement between the simulation results in Fig. 2 and Eqs. (12) and (13) was observed. These results were obtained with the particle electron number and parallel flux densities n_e^n and $j_{e\parallel}^n$ used in Eqs. (4) and (5).

C. Ion-temperature-gradient instability

We also have tested the implicit-moment δf algorithm on simulations of the ion-temperature-gradient instability. Two-dimensional kinetic simulations with a fully nonlinear gyrokinetic ion and drift-kinetic electron algorithm were first reported by Lee and Tang [19]. Cohen and Williams reported simulations of the same ITG case with fully nonlinear gyrokinetic ions and subcycled drift-kinetic electrons using an explicit integration scheme, and with subcycled, orbit-averaged drift-kinetic electrons using a semi-implicit integration scheme [11].

In Figs. 3 and 4 we display the results of ITG simulations in a shearless slab using the implicit-moment δf algorithm. Results for isothermal fluid electrons ($p_{e\parallel}=n_ev_e^2$) are shown in Fig. 3. Drift-kinetic electrons were used to obtain the results in Fig. 4. The simulation parameters were $L_n/L_T=4$ for each species, $T_i=T_e$, $\rho_i/L_n=0.05$, $16\Delta x\times16\Delta y$, $\Delta x=\Delta y=\rho_i$, $B_y/B_0=0.01$, $\epsilon_1=\epsilon_2=\epsilon_3=0.65$, $\omega_h\Delta t_i=0.933$, $\exp(-k^4a^4)$ smoothing with $a=0.9$, $\omega_{pe}\Delta t_i=4000$, $m_i/m_e=1836$, $\Omega_{ce}/\omega_{pe}=1$, $n_0=64/\Delta x^2$, and $\Delta t_i/\Delta t_e=5$. Modes with $k_y=0$ and $|k|>10\pi/16\Delta y$ were suppressed in the electric potential. In the linear phase for both simulations, the modes with

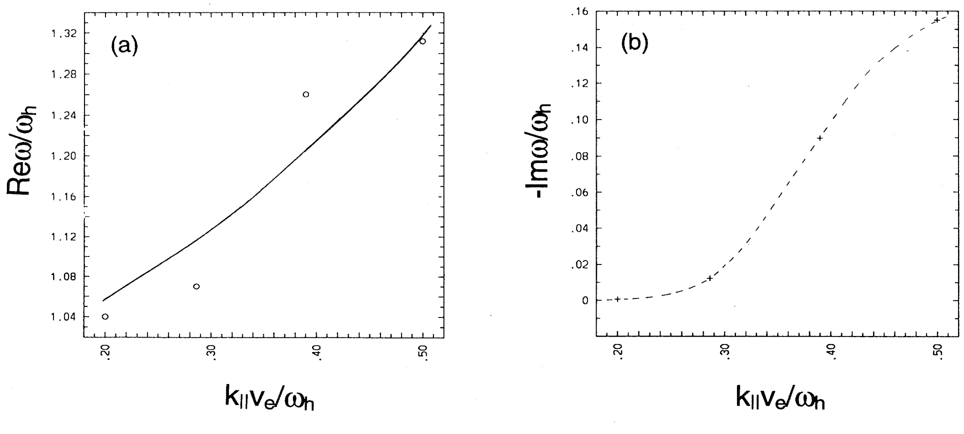

FIG. 2. The dispersion relation for a warm-plasma ω_h mode and test simulation results for (a) $\mathrm{Re}\,\omega/\omega_h$ and (b) $-\mathrm{Im}\,\omega/\omega_h$ vs $k_\parallel v_e/\omega_h$. The solid and dotted curves indicate analytical theory.

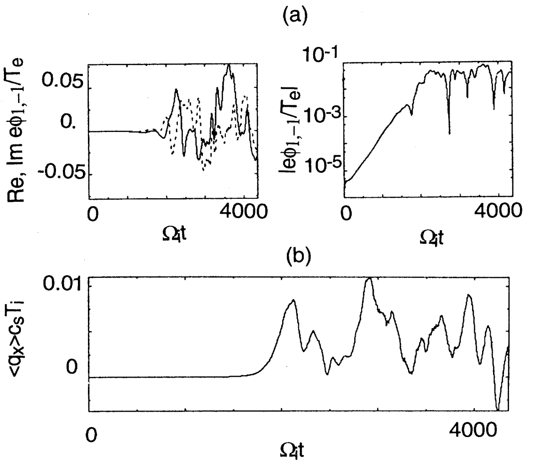

FIG. 3. Ion-temperature-gradient simulation results with an isothermal fluid electron model using the implicit-moment δf algorithm. (a) Re, Im, and absolute value of $e\phi_{1,-1}/T_e$ vs Ωt_i. (b) Spatially averaged ion cross-field thermal transport rate $\langle q_x \rangle / c_s T_i$ vs $\Omega_i t$.

$(k_x, k_y) = (1, \pm 1)(2\pi/16\Delta y)$ exhibited the fastest growth rates, $\omega/\Omega_i = \mp 0.006 + i0.0046$ compared to the theoretical expectation $\omega/\Omega_i = \mp 0.006 + i0.0046$. Because $k_{\parallel} v_e / \Omega_i \approx 0.2 >> |\omega/\Omega_i|$, the influence of electron kinetics on the linear dispersion of the ITG mode in this instance is small.

The results in Figs. 3 and 4 should be compared to Fig. 2 of Lee and Tang [19] and Figs. 5, 6, and 7 of Cohen and Williams [11]. The cross-field ion thermal transport in Figs. 3 and 4 are similar, but the fluid electron case has a higher peak transport rate; and in the kinetic case it subsides more quickly as was observed by Lee and Tang [19]. It should be noted that the nondimensional spatially averaged ion thermal diffusivity in gyro-Bohm units $(\chi_{\rm GB} \equiv \rho_s^2 c_s / L_n)$ is $\hat{\chi} = \chi / \chi_{\rm GB} = (L_T L_n / \rho_s^2) \langle q_x \rangle / c_s T_i$, where $\langle q_x \rangle$ is the spatially averaged cross-field ion thermal transport [20]. For a peak value of transport $\langle q_x \rangle / c_s T_i = 0.01$, $\hat{\chi} = 1$ for the parameters of these simulations. The δf ion thermal transport rates are approximately double those in the fully nonlinear simulations. The saturation mechanism in this system is coherent mode coupling [19], and the thermal transport at saturation has been found to be sensitive to both spatial smoothing and the level of background thermal noise. Therefore, it is important to demonstrate convergence of the results. The saturated thermal transport exhibits a highly nonlinear, somewhat chaotic time dependence. We find that the detailed time history of the ion thermal transport after reaching its first peak depends on the values of the parameters controlling the spatial smoothing, the time step, and the centering parameters $\{\epsilon_1, \epsilon_2, \epsilon_3\}$. However, the time-averaged thermal transport rate at saturation displayed here is reasonably converged ($\leq 25\%$ variations).

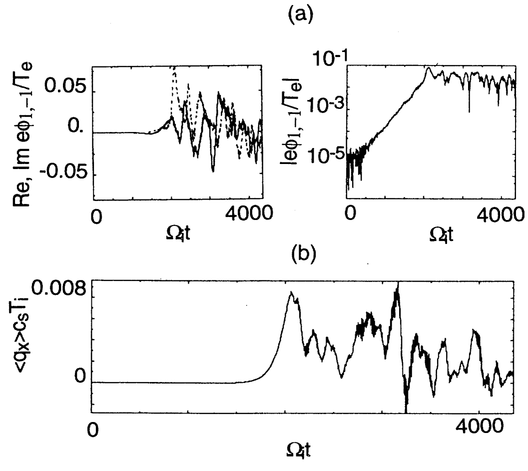

FIG. 4. Ion-temperature-gradient simulation results with drift-kinetic electrons using the implicit-moment δf algorithm. (a) Re, Im, and absolute value of $e\phi_{1,-1}/T_e$ vs $\Omega_i t$. (b) Spatially averaged ion cross-field thermal transport rate $\langle q_x \rangle / c_s T_i$ vs $\Omega_i t$.

As in the simulations of Cohen and Williams [11], the nonlinear $\mathbf{E} \times \mathbf{B}$ velocity at saturation determines the limiting time step in these simulations, $|\mathbf{v}_{\mathbf{E}\times\mathbf{B}}| \Delta t_i / \Delta x \leq 0.2$. The largest time step Δt_i that we could use with either kinetic or fluid electrons was the same. We will return to this point in the next subsection.

D. Collisionless drift instability

Kinetic electron effects are essential to the instability mechanism in the collisionless drift instability [2,21]. Inverse electron Landau damping and a density gradient lead to an instability in an unsheared configuration. Two-dimensional unsheared simulations of the collisionless drift instability provide a rigorous test of our kinetic electron algorithm.

Figures 5, 6, and 7 show results from implicit-moment δf simulations with $T_e/T_i = 4$, $\rho_s/L_n = 0.214$, $m_i/m_e = 1837$, $\Omega_e/\omega_{pe} = 10$, $\lambda_e/\Delta x = 1$, $\rho_s/\Delta x = 4$, $B_y/B_0 = 0.01$, $32\Delta x \times 32\Delta y$, $\omega_{pe}\Delta t_i = 200$, and $\Delta x = \Delta y$. Solutions of the linear dispersion relation are given by Lee *et al.* [21] Modes $(k_x, k_y) = (1, \pm 1)$ in units of $2\pi/L$ are the fastest growing modes with $\omega/\Omega_i = \pm 0.06 \pm i0.011$, which is what is observed in the simulations, Fig. 5. The earlier simulations of Lee *et al.* [21] used a fully nonlinear algorithm for both ions and electrons with thermal noise levels so high that determination of the linear growth rates was very difficult. Our simulations have much lower noise levels.

The nonlinear behavior of our simulations differs from those of Lee *et al.* For the simulation shown in Fig. 5, the radial modes for the electric potential ($k_y = 0$, $k_x \neq 0$) and all modes with $k_x = 0$ were suppressed; and the multiscale model without the nonlinear correction suggested in the work of Lee *et al.* [3,21] was used. The retention of the higher-order nonlinear term associated with the equilibrium spatial gradients can influence the saturation of the drift-wave instability [22]. In the simulations of Lee *et al.* [21], the fastest growing mode reached max-

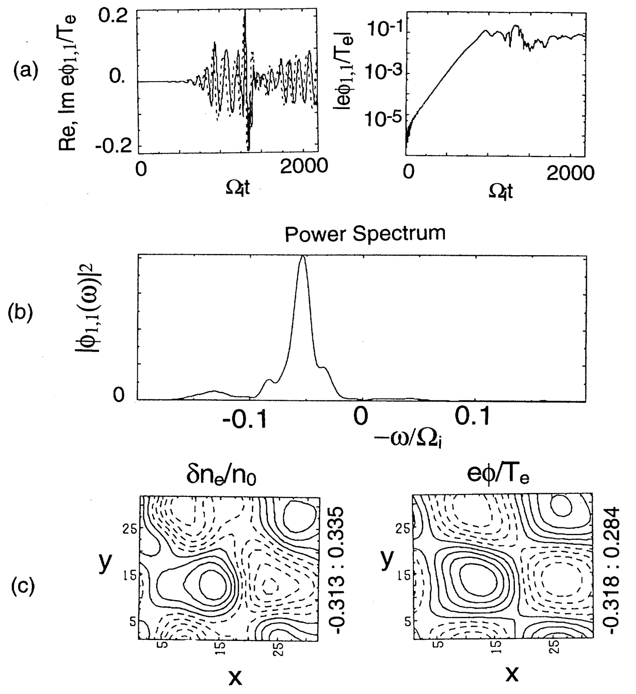

FIG. 5. Collisionless drift instability in a $32\Delta x \times 32\Delta y$ system with no radial modes. (a) Re, Im, and absolute value of $e\phi_{1,1}/T_e$ vs $\Omega_i t$. (b) Power spectrum for the $(1,-1)$ mode. (c) Contour plots of electron density perturbation and $e\phi(x,y)/T_e$ at the end of the simulation.

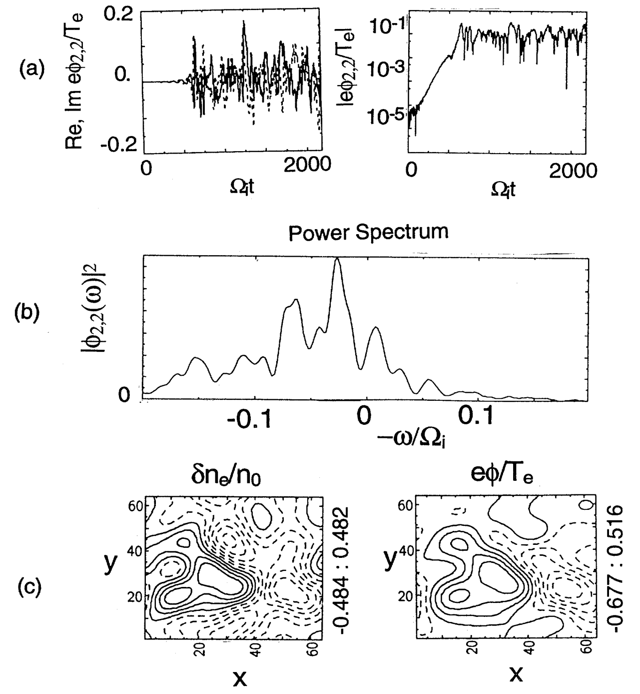

FIG. 7. Collisionless drift instability in a $64\Delta x \times 64\Delta y$ system with radial modes. (a) Re, Im, and absolute value of $e\phi_{2,2}/T_e$ vs $\Omega_i t$. (b) Power spectrum for the (2,2) mode. (c) Contour plots of electron density perturbation and $e\phi(x,y)/T_e$ at the end of the simulation.

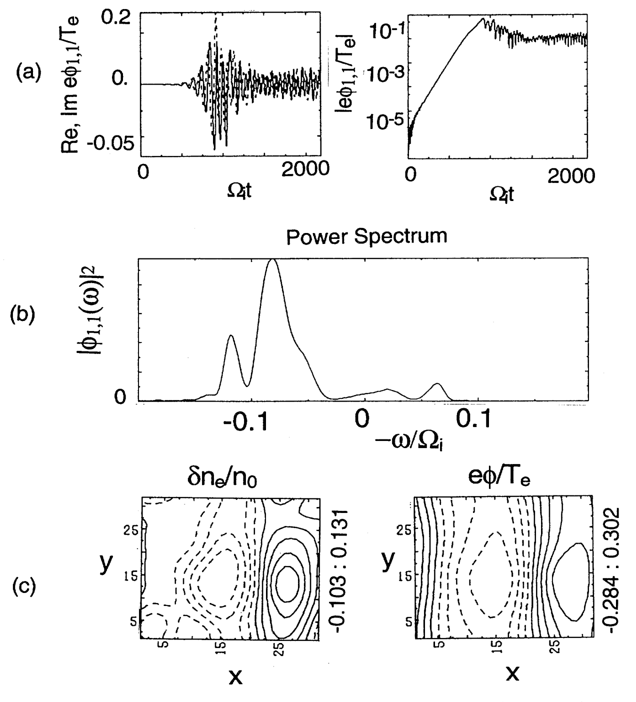

FIG. 6. Collisionless drift instability in a $32\Delta x \times 32\Delta y$ system with radial modes. (a) Re, Im, and absolute value of $e\phi_{1,1}/T_e$ vs $\Omega_i t$. (b) Power spectrum for the (1,1) mode. (c) Contour plots of electron density perturbation and $e\phi(x,y)/T_e$ at the end of the simulation.

imum amplitudes $|e\phi/T_e| \approx 1\%$, while the amplitudes in our simulations peaked at amplitudes approaching mixing-length amplitudes, $|e\phi/T_e| = 0.1-0.2$, and then subsided. The mixing-length estimate of the saturation of the fastest growing modes gives $|e\phi/T_e| = 1/k_x L_n \approx 0.25$ for the parameters of this simulation.

In Fig. 6 we show results from a simulation of a collisionless drift instability with the same physical parameters as in Fig. 5, but with the radial modes ($k_x \neq 0$, $k_y = 0$) included. The inclusion of radial modes allows the nonlinear generation of sheared $\mathbf{E} \times \mathbf{B}$ flow via nonlinear convective steepening that can have a profound stabilizing effect on drift-wave instabilities when the spread in the Doppler-shifted mode frequency over the mode width in x is comparable to or greater than the mode growth rate [20,23]. With radial modes in the simulation, Fig. 6 indicates the fastest growing modes peaked at $|e\phi/T_e| \sim 0.05$ and subsided to $0.01-0.02$ amplitude. This system evolves in a relatively coherent manner, the fastest-growing modes peaking in amplitude and then relaxing substantially as long-wavelength radial modes grow nonlinearly to a significant amplitude $|\delta n_e(x)/n_0| \approx 0.15$ and produce a substantial sheared flow.

A more turbulent saturated state arises when the system size is increased to $64\Delta x \times 64\Delta y$ in Fig. 7. The mode with the same wave number in the bigger system as the fastest growing mode in the smaller system exhibited the same growth rate and frequency, and saturated at $|e\phi/T_e| \sim 0.01-0.02$ with radial modes included without the overshoot and relaxation observed in the smaller system. Fig. 6. The sheared flow generated has even larger amplitude $|\delta n_e/n_0| \approx 0.5$ and a more turbulent structure in space. There are significant nonlinear frequency shifts observed in the power spectra and a loss of coherence accompanying saturation.

We studied the convergence of the drift-wave simulation of the larger, more turbulent system with respect to particle number, time step, and the ratio $\Delta t_i/\Delta t_e$. We kept the number of electrons and singly charged ions equal to one another in all cases; however, this could be varied as well. For the $64\Delta x \times 64\Delta y$ collisionless drift-wave case, we were able to reduce the number of simulation particles to $n_0 = 4/\Delta^2$ and obtain consistent results with good signal-to-noise properties. Lee *et al.* [21] used $n_0 = 16/\Delta^2$ in their nonperturbative simulations with much inferior signal-to-noise ratio in their results. The largest field-solve time step that we found acceptable for this case was $\omega_{pe}\Delta t_i = 400$ [$\omega_h \Delta t_i = 0.933$, $\Omega_i \Delta T_i = 2.2$, $(B_y/B_0)v_e \Delta t_i/\Delta x = 3.74$] and was limited by the particle Courant condition for the $\mathbf{E}\times\mathbf{B}$ velocity, $v_{\mathbf{E}\times\mathbf{B}}\Delta t_i/\Delta x \leq 0.2$. The largest time step that we could use for either a fluid or kinetic electron model was the same. Lee *et al.* quote a time step of $\omega_{pe}\Delta t = 200$ for this case. Our simulation results were essentially the same for $N \equiv \Delta t_i/\Delta t_e = 2$, 5, or 10 and $\omega_{pe}\Delta t_i = 400$. We attribute the insensitivity of the simulation results to the electron subcycling parameter $\Delta t_i/\Delta t_e$ to the relatively small value of Δt_i set by the nonlinearity here and because only $\langle p_{e\parallel} \rangle$ is orbit averaged. From the perspective of computational cost, the simulation with $N = 2$ is the most efficient.

IV. DISCUSSION

In this paper we have introduced an algorithm for efficient simulation of collective phenomena in a plasma where both ion and electron kinetics are retained. We specialized to a strongly magnetized plasma with gyrokinetic ions and drift-kinetic electrons. We performed a simple analysis of the dispersion characteristics of the highest-frequency normal mode for a finite time step and confirmed the analysis with simulations. We also verified that the algorithm correctly recovers electron Landau damping and the linear dispersion relations for simple limits of the ion temperature gradient and collisionless drift instabilities in a two-dimensional, unsheared slab.

The ITG and collisionless drift-wave simulations were compared to earlier reported work with a nonperturbative, fully nonlinear kinetic algorithm and found to have superior signal-to-noise properties. The nonlinear evolution of these simulations exhibited a transition from relatively coherent mode coupling-phenomena [21,22] when the spatial resolution is relatively sparse, to more turbulent nonlinear saturations when the system size was increased with the cell size held constant so that the number of modes was substantially increased ($\times 4$). As in other slab simulations of ITG and collisionless drift-wave instabilities, the saturated states in our simulations showed significant nonlinear frequency shifts, turbulent $\mathbf{E}\times\mathbf{B}$ trapping, and self-generated shear flows that were strongly stabilizing when radial modes were allowed.

We find that the improvement in simulation efficiency in our two-dimensional ITG and collisionless drift instability computations is dependent on the specific physics application. The use of the δf method leads to a substantial reduction in the particle requirement. We were routinely able to use substantially fewer particles than in fully nonlinear, nonperturbative simulations (e.g., $\frac{1}{4}$ the number of particles), while achieving much quieter simulations (the actual reduction in particles for comparable signal to noise would have been much larger). The simulation costs of the implicit-moment δf method are divided as follows. The drift-kinetic particle push with one electron moment accumulated is $\sim\frac{1}{5}$ of the gyrokinetic particle push with one accumulation. The implicit-moment algorithm requires two additional electron moments accumulated on each time step, which is optimized on a vector computer using a method much like that of Heron and Adam [24] and adds another $\sim 50\%$ to the cost of the electron push. Thus, in the particle-dominated case with subcycling parameter $N = 5$, the inclusion of drift-kinetic electrons increases the calculation cost to 250% of the cost with adiabatic fluid electrons. If the δf reduction in particle number is so profound that the simulation is no longer particle dominated, then the field solve becomes more important in the computational cost inventory, and the inclusion of drift-kinetic electrons increases the total cost by less than quoted in the preceding. We note that in the collisionless drift-wave simulations, the inclusion of drift-kinetic electrons with $N = 2$ and realistic ion-electron mass ratio resulted in an additional 50–60 % computational cost.

The simulation experience presented here demonstrates the efficacy of combining multiple time scale and perturbative methods: implicitness, δf, subcycling, gyrokinetics, and drift kinetics. These techniques facilitate simulations of kinetic ion and electron plasmas with realistic mass ratios and with unprecedented computational efficiency in our experience. It is our intention to extend the application of this method to three-dimensional, toroidal configurations and to include electromagnetic coupling [17]. Cummings has already successfully demonstrated the combination of the δf method with electron subcycling in a two-dimensional slab electromagnetic model for simulating drift-wave turbulence [25].

ACKNOWLEDGMENTS

We are grateful to X. Xu for useful discussions and assistance. This work was performed for the U.S. Department of Energy under Contract No.W-7405-ENG-48 at the Lawrence Livermore National Laboratory and contributes to the Numerical Tokamak Project, which is an activity supported jointly by the U.S. Department of Energy's Office of Fusion Energy and the Mathematics, Information, and Computational Sciences Division as part of the High Performance Computing and Communications Program.

[1] *Multiple Time Scales,* edited by J. U. Brackbill and B. I. Cohen (Academic, Orlando, 1985).

[2] W. M. Tang, Nucl. Fusion **18**, 1089 (1978).

[3] W. W. Lee, J. Comput. Phys. **72**, 243 (1987).

[4] J. C. Adam, A. Gourdin-Serveniere, and A. B. Langdon, J. Comput. Phys. **47**, 229 (1982).

[5] B. I. Cohen, (Ref. [1]), Chap. 10.

[6] M. Kotschenreuther, Bull. Am. Phys. Soc. **34**, 2107 (1988); (private communication); in *Proceedings of the 14th International Conference on the Numerical Simulation of Plasmas* (SAIC-NRL, Annapolis, MD, 1991); R. E. Denton and M. Kotschenreuther, J. Comput. Phys. **119**, 283 (1995).

[7] A. M. Dimits and W. W. Lee, J. Comput. Phys. **107**, 309 (1993).

[8] J. Denavit, J. Comput. Phys. **42**, 337 (1981).

[9] R. J. Mason, Phys. Fluids **23**, 2204 (1980); J. Comput. Phys. **41**, 233 (1981); Phys. Rev. Lett. **47**, 652 (1981).

[10] J. U. Brackbill and D. W. Forslund, in *Multiple Time Scales* (Ref. [1]), Chap. 9.

[11] B. I. Cohen and T. J. Williams, J. Comput. Phys. **107**, 282 (1993).

[12] D. C. Barnes and R. A. Nebel, Bull. Am. Phys. Soc. **36**, 2433 (1991).

[13] E. A. Frieman and Liu Chen, Phys. Fluids **25**, 502 (1982).

[14] W. W. Lee, Phys. Fluids **26**, 556 (1983).

[15] G. Hu and J. A. Krommes, Phys. Plasmas **1**, 863 (1994).

[16] S. E. Parker and W. W. Lee, Phys. Fluids B **5**, 77 (1993).

[17] X. Q. Xu, B. I. Cohen, A. M. Dimits, and J. A. Byers, Bull. Am. Phys. Soc. **38**, 2016 (1993).

[18] C. K. Birdsall and A. B. Langdon, *Plasma Physics via Computer Simulation* (McGraw-Hill, New York, 1985).

[19] W. W. Lee and W. M. Tang, Phys. Fluids **31**, 612 (1988).

[20] B. I. Cohen, T. J. Williams, A. M. Dimits, and J. A. Byers, Phys. Fluids B **5**, 2967 (1993).

[21] W. W. Lee, J. H. Krommes, C. R. Oberman, and R. A. Smith, Phys. Fluids **27**, 2652 (1984).

[22] A. M. Dimits, Ph.D. thesis, Princeton University, 1988.

[23] A. Hassam, T. M. Antonsen, Jr., J. F. Drake, and C. S. Liu, Phys. Rev. Lett. **66**, 309 (1991).

[24] A. Heron and J. C. Adam, J. Comput. Phys. **85**, 284 (1989).

[25] J. C. Cummings, Ph.D. thesis, Princeton University, 1995.